Autogenous shrinkage and sustainability assessment of alkali-activated slag incorporating steel slag

Li, Kang; Yang, Zhengxian; Nicolaides, Demetris; Liang, Minfei; Briseghella, Bruno; Marano, Giuseppe Carlo; Zhang, Yong

DOI
10.1016/j.conbuildmat.2024.137219

Publication date
2024

Document Version
Final published version

Published in
Construction and Building Materials

Construction and Building Materials 438 (2024) 137219

Contents lists available at ScienceDirect

Construction and Building Materials

journal homepage: www.elsevier.com/locate/conbuildmat

Autogenous shrinkage and sustainability assessment of alkali-activated slag incorporating steel slag

Kang Li [a], Zhengxian Yang [a], Demetris Nicolaides [a,b], Minfei Liang [c], Bruno Briseghella [a], Giuseppe Carlo Marano [d], Yong Zhang [a,*]

[a] Joint International Research Laboratory of Deterioration and Control of Coastal and Marine Infrastructures and Materials, College of Civil Engineering, Fuzhou University, Fuzhou 350108, China
[b] Department of Civil Engineering, Frederick University, Nicosia 1036, Cyprus
[c] Faculty of Civil Engineering and Geosciences, Delft University of Technology, Delft 2628 CN, the Netherlands
[d] Department of Structural, Geotechnical and Building Engineering, Politecnico di Torino, Corso Duca degli Abruzzi, 24, Torino 10129, Italy

ARTICLE INFO

Keywords:
Autogenous shrinkage
Chemical shrinkage
Alkali-activated slag
Steel slag
Hydration
Sustainability

ABSTRACT

This paper presents a comprehensive investigation on the positive potential of steel slag (SS) to mitigate the autogenous shrinkage of alkali-activated slag (AAS) while maintaining a reasonably high strength. Changes of the physicochemical properties of AAS with the addition of SS were examined in terms of hydration heat, autogenous shrinkage, chemical shrinkage, internal relative humidity (RH) and mechanical behaviors. The microstructure of AAS-SS systems was characterized using X-ray diffraction, thermogravimetric analysis and nitrogen adsorption techniques. The shrinkage mechanism and quantification approach of the AAS-SS systems were discussed, in addition to a sustainability assessment. The results indicate that the 7-day autogenous shrinkage of AAS paste was decreased by 16 %, 35 % and 42 % when SS was incorporated by 15 %, 30 % and 45 % respectively, owing to the obviously slower hydration and higher internal RH at the early age. Meanwhile, the inclusion of SS substantially mitigates the chemical shrinkage and reduces the pores below 50 nm, thereby significantly decreasing the capillary pressure associated with smaller water-filled pore sizes. Substitutions of blast furnace slag by up to 45 % SS enable to reduce CO_2 emissions by 18.4 kg/m^3 and decrease autogenous shrinkage by 42 % without obvious compromise in the loss of elastic modulus and compressive strength.

1. Introduction

The construction sector serves as a pivotal driver of the global economy and environment. With the ongoing acceleration of urbanization, the demand for construction materials is steadily increasing [1,2]. Nonetheless, the construction sector remains a notable contributor to greenhouse gas emissions, primarily owing to the substantial CO_2 footprint stemming from ordinary Portland cement (OPC) production and concrete utilization [3–5]. Addressing the challenge of climate change necessitates the urgent quest within the construction industry for environmentally friendly and sustainable building materials. Alkali-activated slag (AAS), which serves as a clinker-free substitute for conventional cement, is produced through mixing the blast furnace slag (BFS) with an alkaline activator [6,7]. This helps to reduce the construction industry's dependence on limited natural resources and alleviate ecological stress, while also lowering the carbon footprint of the industry [8–10]. In addition, the AAS excels in mechanical properties and chemical resistance, which makes AAS concrete structures more stable and durable [11–13]. These characteristics provide more design freedom for construction projects and are expected to reduce maintenance costs.

AAS poses some challenges as well. One of them is its fast-setting property [14], which may cause inconvenience in construction work. Another thorny issue is the high autogenous shrinkage, which tends to cause cracking in concrete [15]. Earlier investigations have demonstrated that AAS exhibits 5–7 times greater shrinkage compared to OPC when cured under sealed conditions [16,17]. Over recent decades, researchers have extensively investigated the autogenous shrinkage of AAS. Nonetheless, consensus regarding the mechanism underpinning this significant autogenous shrinkage remains elusive. Surface tension, disjoining pressure and tension in capillary water are recognized to be the driving forces for autogenous shrinkage [18]. Notably, capillary

* Correspondence to: College of Civil Engineering, Fuzhou University, Fuzhou 350116, China.
E-mail address: y.zhang@fzu.edu.cn (Y. Zhang).

https://doi.org/10.1016/j.conbuildmat.2024.137219
Received 12 May 2024; Received in revised form 21 June 2024; Accepted 23 June 2024
Available online 27 June 2024

pressure is particularly favored due to its foundation in robust mechanical and thermodynamic considerations [16,19]. Throughout the hydration process, free water within the matrix gradually diminishes, inducing self-desiccation within the cement paste and subsequent reduction in internal relative humidity (RH). This process results in the decrement of water-filled capillary pores within the hardened cement paste, accompanied by a decrease in pore water saturation. When the capillaries shift from saturated to unsaturated, internal pressure is exerted on the concave surfaces of the pores. To maintain equilibrium of the concave surface, capillary tension increases and hence causing autogenous shrinkage.

Collins and Sanjayan [20] found that OPC pastes comprised 36.4 % mesopores along with a substantial portion of macropores. In contrast, waterglass (WG) activated AAS pastes exhibited as much as 80 % mesopores, contributing to the elevated autogenous shrinkage of AAS. As reported in [21], the AAS exhibited greater autogenous shrinkage compared to OPC owing to the much finer capillary pores in AAS. Cartwright et al. [22] arrived at similar conclusions in their research. Additionally, RH was identified as a primary factor influencing autogenous shrinkage. On the basis of Song et al. [23], the higher autogenous shrinkage of AAS was typically a result of larger reductions in the RH, pointing to a RH-dependent autogenous shrinkage.

Several strategies have been proposed to reduce the autogenous shrinkage of AAS system. As claimed in literature [24,25], the utilization of superabsorbent polymer (SAP) has effectively mitigated the autogenous shrinkage of AAS. The SAP establishes a water reservoir layer in the AAS system, supplying additional water during hydration to counteract water depletion and retard self-desiccation [26]. However, this approach suffers from the major issue of reducing the compressive strength at early ages [27,28]. Except for SAP, the incorporation of shrinkage-reducing admixture can suppress the shrinkage stresses generated during capillary pore water loss through reducing the surface tension and interfacial energy of pore water [29]. As described elsewhere [30], although gypsum incorporations alleviated the shrinkage at the initial stage, this early expansion was difficult to offset the subsequent long-term shrinkage due to the limited compensation of the expansion phase. Previous reports suggested that the deformation of C-A-S-H gels can be altered by increasing the curing temperature, thereby reducing autogenous shrinkage of AAS [30,31]. This approach, however, is not applicable in cast-in-place concrete. Furthermore, high-temperature curing can result in higher energy consumption and a larger carbon footprint, contradicting sustainable building principles.

Introducing alternative precursors for concurrent activation with BFS is deemed an effective solution. Steel slag (SS), a by-product accompanying the steel smelting process, is produced in China at an annual rate surpassing 100 million tons. However, its utilization rate remains below 30 % [32,33]. A significant volume of discarded SS accumulates on land, resulting in resource wastage and environmental pollution [34,35]. Conventionally, SS undergoes natural cooling, leading to its low reactivity [36,37]. Research indicates that employing mineral admixtures with lower reactivity holds promise in controlling the autogenous shrinkage of AAS [38,39]. Meanwhile, the presence of SS could result in higher workability, longer setting time and lower chloride diffusion coefficient [38,40]. This paper aims to obtain basic insights into the mechanisms of SS in reducing the autogenous shrinkage of AAS paste. The impacts of incorporating SS into AAS were investigated in terms of setting time, hydration heat, hydration products, pore structure, RH, chemical shrinkage, autogenous shrinkage and mechanical properties. Furthermore, the sustainability of the AAS-SS pastes was evaluated. The research findings provide a reasonable reference for promoting the exploitation of green construction materials utilizing composite BFS/SS materials.

2. Experimental

2.1. Materials

BFS and SS served as the primary precursors for preparing the alkali-activated paste. Table 1 displays the chemical compositions of BFS and SS as determined through X-ray fluorescence (XRF) analysis. Fig. 1 presents the XRD patterns of BFS and SS. Notably, the XRD pattern of BFS exhibits a broad peak spanning from 25° to 40°, indicative of a substantial presence of amorphous phases. In contrast, SS predominantly consists of cementitious components like C_3S and C_2S, along with inert RO phases. Fig. 2 depicts the particle size distribution of BFS and SS. The alkaline activator was formulated by blending sodium hydroxide (with a purity of ≥99 %) with industrial sodium silicate solution (with an original modulus of 3.3, comprising 26.5 wt% SiO_2 and 8.3 wt% Na_2O), along with deionized water.

2.2. Sample preparation

Table 2 displays the mixture design of the pastes. The Na_2O dosage was 6 % by mass of the precursor. The relative amounts of sodium hydroxide and sodium silicate were adjusted to achieve a molar ratio of SiO_2/Na_2O was 0.93. If the SiO_2 and Na_2O in the activator were regarded as solids, the alkali-activated paste had a liquid-binder (l/b) ratio of 0.5 and a water-solid (w/s) ratio of 0.35. Note that the activator was fabricated one day prior to casting to ensure a solution of ambient temperature. During the mixing process, the raw materials were initially pre-mixed for 60 s, then the alkaline activator was added with low speed for 90 s and high-speed for another 90 s.

2.3. Test methods

2.3.1. Setting time

According to ASTM C191–21, the initial and final setting times of the paste were tested using a Vicat needle.

2.3.2. Hydration heat

The hydration heat of the paste was monitored using a TAM air isothermal calorimeter at 20 °C. Pre-mixed fresh paste (approximately 10 g) was quickly injected into an ampoule using a syringe, which was then sealed and placed in the channel of the calorimeter. Calorimetric results were normalized according to the precursor weights.

2.3.3. Autogenous shrinkage

The autogenous shrinkage of the paste was tested by the corrugated tube method following ASTM C1698–19. Fresh paste was poured into corrugated tubes with 425 ± 0.5 mm in length and 29 ± 0.5 mm in diameter. A vibrating table was turned on throughout the pouring procedure to allow the paste to fulfill the tubes. Following that, the end plug was screwed on, any excess paste on the surface was cleaned with a damp cloth, and the specimens were positioned horizontally on a test stand. The autogenous shrinkage of the samples was recorded at 0.25 h intervals from final setting time to 168 h. Three replicate tests were carried out for each mixture.

2.3.4. Chemical shrinkage

The chemical shrinkage of the paste was tested by the volumetric method outlined in ASTM C1608–17. The fresh paste was poured into a 300 ml Erlenmeyer flask for a thickness of about 5–10 mm. Next, the Erlenmeyer flask was filled with de-aerated water and a perforated rubber stopper was inserted afterwards. Then a glass pipette of 10 ml with a scale of 0.01 ml was placed into the rubber stopper. After adjusting the height of the liquid in the pipette, 1–2 drops of paraffin oil were injected above the liquid to prevent water loss. Finally, the entire setup was placed in a water bath at 23±1 °C and the water level readings on the pipette were recorded periodically. Chemical shrinkage *CS(t)* was

Table 1
Chemical compositions of BFS and SS (wt%).

Oxides	SiO_2	CaO	Al_2O_3	Fe_2O_3	MgO	SO_3	K_2O	P_2O_5	Other	LOI
BFS	34.50	34.00	17.70	1.03	6.01	1.64	0.36	-	3.92	0.84
SS	20.92	40.44	6.22	20.24	5.43	0.25	0.52	0.76	3.34	1.88

LOI = Loss on ignition.

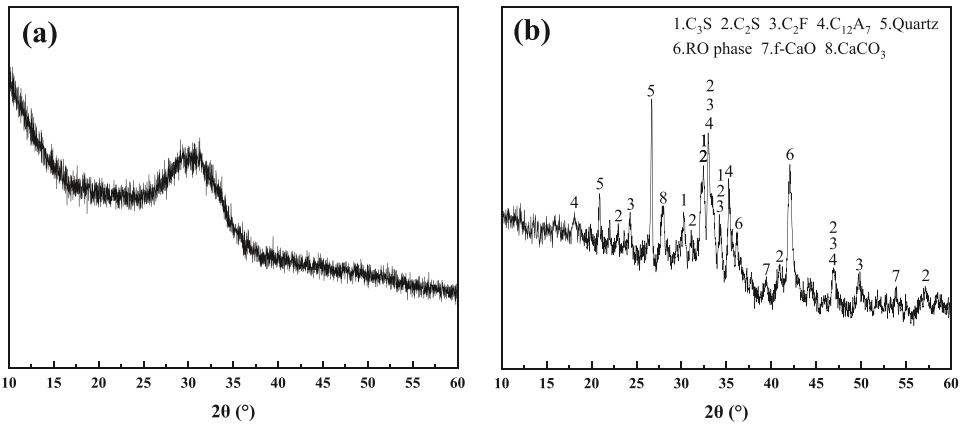

Fig. 1. XRD patterns of (a) BFS and (b) SS.

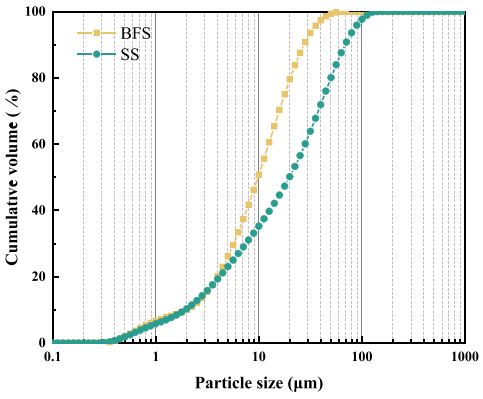

Fig. 2. Particle size distribution of BFS and SS.

Table 2
Mix design of the pastes.

Mix ID	BFS (g)	SS (g)	SiO_2 (mol)	Na_2O (mol)	H_2O (g)
100BFS	646	–	0.58	0.63	250.4
85BFS15SS	549.1	96.9	0.58	0.63	250.4
70BFS30SS	452.2	193.8	0.58	0.63	250.4
55BFS45SS	355.3	290.7	0.58	0.63	250.4

calculated using Eq. (1):

$$CS(t) = \frac{h(t) - h(0)}{M_{\text{binder}}} \quad (1)$$

where M_{binder} (g) is the mass of binder, while *h(0)* (ml) and *h(t)* (ml) are the readings of the liquid height in the pipette at the time of 0 and t, respectively.

2.3.5. Internal relative humidity

The internal RH of the paste was monitored using a JWSL-6A humidity sensor with a rod probe. The configuration of the RH measurements is schematically illustrated in Fig. 3. Cubic paste samples 100 mm

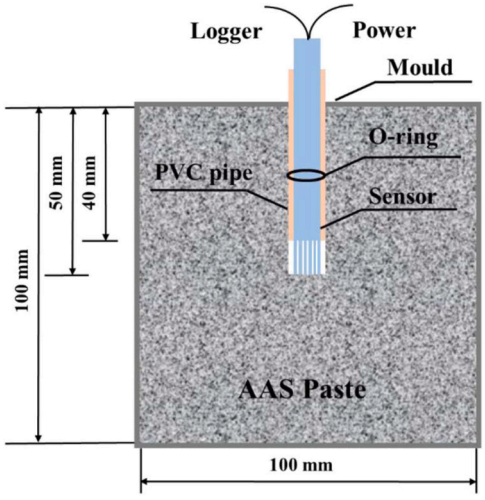

Fig. 3. Schematic diagram of internal relative humidity measurement.

× 100 mm × 100 mm were prepared. During casting, a PVC pipe was pre-buried inside the specimen. The PVC pipe was pre-positioned with an aluminum bar in close contact with its inner wall, and the length of the aluminum bar extended 10 mm beyond the top and bottom of the PVC pipe. After the initial setting of the specimen, the aluminum bar was slowly withdrawn and then the sensor was immediately placed in the PVC pipe. Simultaneously, a 2 mm-thick O-ring was used to ensure tightly contact between the pipe and the sensor. A sealing film was applied to seal the gap between the top of the PVC pipe and the sensor for preventing water evaporation. It is worth noting that the humidity sensors need to be calibrated using different types of saturated salt solutions before measurement. Three parallel measurements of each mixture were carried out.

2.3.6. Mechanical properties

The compressive strength of the paste, prepared in the mold 40 mm × 40 mm × 40 mm, was determined at 1, 7 and 28 days following the Chinese standard GB/T 17671–2021. Three parallel samples of each

mixture were tested. The elastic modulus of the paste was tested on the specimens at 1 day and 7 days according to GB/T50081–2019. Three specimens with dimensions of 40 mm × 40 mm × 160 mm were used for each mixture to measure the elastic modulus.

2.3.7. Microstructure analysis

The crystalline phases of the paste powder were analyzed utilizing X-ray diffraction (XRD). The scanning angle (2θ) ranged from 5° to 60° in steps of 0.02° with a voltage of 40 kV and a current of 40 mA. Solid-phase changes in the paste were determined by thermogravimetric analysis (TGA). The temperature range was 30–1000 °C at a heating rate of 10 °C/min.

The pore structure of the paste was assessed using the nitrogen adsorption method. Paste specimens cured to a desired age were crushed into pieces and then soaked in isopropanol for 3 days to halt hydration. The pieces were placed in a vacuum drying oven at 50 °C until constant weight. Nitrogen adsorption tests were carried out on an ASAP 2460 Porosimetry system (Micromeritics, USA), with relative pressures in the range of 0.05–0.998. Pore size distributions were deduced from the nitrogen adsorption data using the Barrett-Joyner-Halenda (BJH) model [41].

2.4. Sustainability assessment

Developing environment-friendly construction materials is crucial to ensure long-term sustainability. The environmental and economic dimensions of mixtures were evaluated utilizing the life cycle assessment (LCA). The transportation distance of each material was included in the LCA. To reduce transportation costs, the raw materials are often sourced from the closest locations. For each material the emissions during mixing and curing were considered equal, which were not involved in the calculation. Table 3 gives a list of the items for the sustainability assessment. The BFS was easier to grind than SS, and the electricity consumption for grinding BFS and SS was approximately 45 kW·h/t and 60 kW·h/t, respectively. The total CO_2 emissions and cost of each raw material were calculated based on the methodology reported in the literature [42].

3. Results

3.1. Setting time

Table 4 displays the results of setting time measurements for AAS paste. The control group (100BFS) exhibited the fastest initial setting time of 20 min, while the final setting time was recorded at 31 min. Increasing the replacement of BFS with SS increased the setting time. At a dosage of 45 % SS (55BFS45SS), the initial and final setting times were increased by 120 % and 170 %, respectively, compared to those of the control group. This was ascribed to the poor reactivity and slow dissolution of SS during the pre-reaction period [38]. In addition, the BFS had a total SiO_2 to Al_2O_3 mass ratio of 1.95, compared to an obviously higher value of 3.36 in the SS. Previous research has indicated that reducing aluminum silicate content or increasing the mass ratio of SiO_2 to Al_2O_3 could result in a prolonged setting time in geopolymers [43].

Table 3
Details of the sustainability assessment for the materials used.

Items	Amount
Truck speed, km/h	80
Truck load, ton	1.0
Diesel consumption, liter/km	0.1
Diesel price, $/liter	1.03
Transport charge, $/km	0.24
Unit power consumption for grinding machine, kW·h/ton	45–60
Electricity price, $/kW·h	0.08
CO_2 emission for 1 liter diesel, ton	0.0026
CO_2 emission for 1 kW·h electricity, ton	0.0003

Table 4
Setting time of AAS-SS pastes.

Mix ID	100BFS	85BFS15SS	70BFS30SS	55BFS45SS
Initial setting (min)	20	22	29	44
Final setting (min)	31	38	63	84

3.2. Hydration heat

Isothermal calorimetry was carried out to evaluate the reaction kinetics of AAS-SS pastes. The results are provided in Fig. 4. For a clear analysis, the heat flow curves are plotted for the first 24 h and the cumulative heat for the entire measurement cycle of 72 h is given. Within the first few minutes, the first peak seen in Fig. 4(a) appears, which is caused by the wetting and early dissolution of the precursor. Afterwards, a second peak indicative of the accelerated hydration stage appears in all curves. This peak signifies the quick production of the primary hydrated gel C-A-S-H. It is noteworthy that substituting BFS by SS postpones the onset of the accelerated stage and diminishes the second peak, with this effect becoming more evident with increasing amounts of SS incorporation. Reducing the early hydration heat is an effective strategy for mitigating temperature-induced shrinkage stresses in concrete structures [18]. The decline in hydration rate following the second peak is commonly associated with the hindrance of precursor dissolution caused by the ongoing generation of C-A-S-H gels around unreacted particles as well as the gradual obstruction of pore space [16]. You et al. [38] found that the heat release of OPC pastes reached approximately 380 J/g within the first 72 h and continued to increase thereafter. In contrast, as depicted in Fig. 4(b), the heat release of AAS pastes over 72 h ranged from 200 to 250 J/g, which was much less than that of OPC pastes. However, in the first 12 h, the hydration heat of the AAS pastes grew rapidly, after which the change of the heat of hydration was slow. It is evident that the strong and rapid chemical reaction of the AAS system occurred in the early stage.

3.3. Autogenous shrinkage

Fig. 5 presents the results of the autogenous shrinkage of AAS-SS pastes. For 100BFS, significant autogenous shrinkage is observed, which is approximately 4900 μm/m after 1 d and reaching 6850 μm/m after 7 d. A clear increase of the autogenous shrinkage can still be observed in between, although the most significant autogenous shrinkage of AAS paste happens during the initial stages of alkali activated reactions. The findings are consistent with those of previous research [17,44]. Introducing 15 % SS as a replacement of BFS results in a reduction of 20 % in the autogenous shrinkage after 1 d and a reduction of 16 % after 7 d. Increasing the SS content to 30 % leads to a decrease of around 35 % in the autogenous shrinkage at both 1 d and 7 d. Further increasing the SS content up to 45 % results in a substantial reduction in the autogenous shrinkage, which is decreased by 43 % after 1 d and by 42 % after 7 d as compared to that of 100BFS at respective ages. It is worthwhile to note that the development of autogenous shrinkage becomes quite slow as elapse of time in the 55BFS45SS with a high amount of SS.

3.4. Chemical shrinkage

Chemical shrinkage refers to the reduction in volume of a paste during the hydration of cementitious materials in cases the volume of resultant hydration products is less than that of the original reactants [45]. Fig. 6 depicts the chemical shrinkage of AAS-SS pastes. Generally, all pastes started with a rapidly increasing trend of chemical shrinkage, especially within the first 24 h, followed by a gradually slow increase of chemical shrinkage. The evolution of chemical shrinkage appeared to

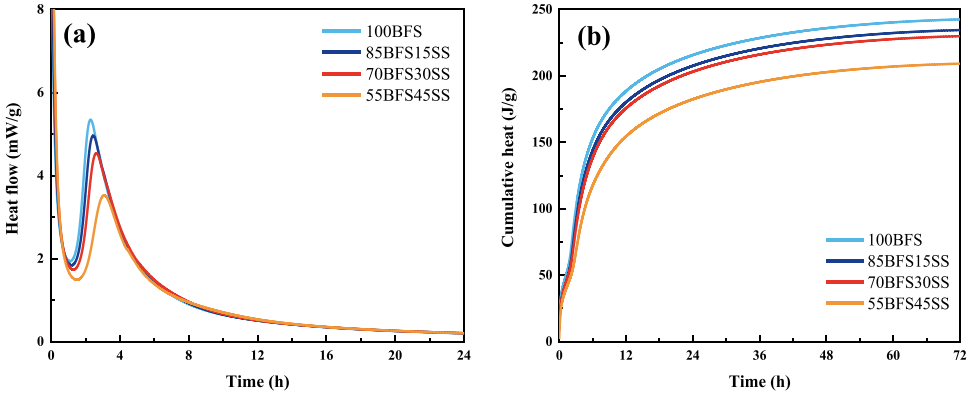

Fig. 4. (a) Heat flow and (b) cumulative heat of AAS-SS pastes.

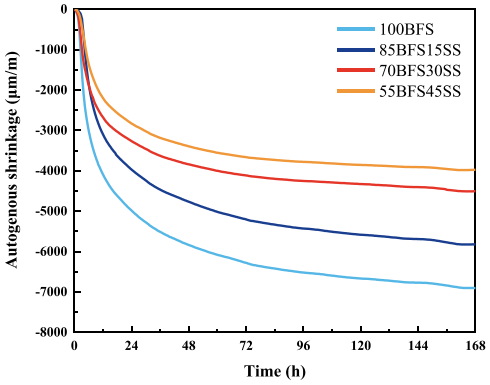

Fig. 5. Autogenous shrinkage of AAS-SS pastes.

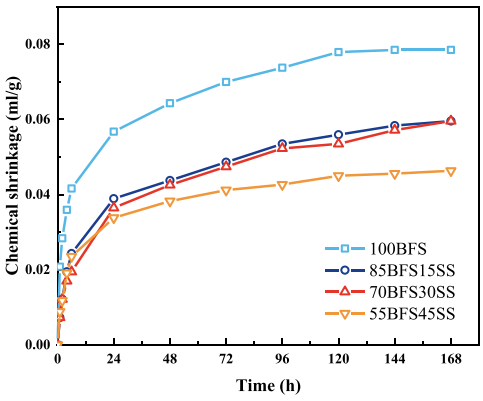

Fig. 6. Chemical shrinkage of AAS-SS pastes.

attain a plateau after 168 h. This was particularly the case for 100BFS, confirming the rapid hydration process of BFS at the early ages. In comparison, AAS pastes containing SS had significantly lower chemical shrinkage than 100BFS without SS at all ages. After 24 h, the chemical shrinkage of paste specimens exhibited a continuously decline trend of chemical shrinkage with increasing SS content. In the first 12 h, a slightly higher chemical shrinkage could be observed for 55BFS45SS. This was straightforwardly associated with the nucleation effect caused by high volume addition of SS and thereby accelerating the hydration progress of BFS at the very early stage. The results of chemical shrinkage agreed with the cumulative heat release data as presented in Fig. 4. The incorporation of SS into AAS reduced the chemical reactivity of entire system. As a result, the transformation of capillary free water into chemically bound water, a main reason leading to chemical shrinkage, was decreased. The poor reactivity of SS, as compared to BFS, along with its slower early hydration reaction, resulted in a low hydration degree. The chemical shrinkage occurs concurrently with the formation of extra voids in the AAS system.

3.5. Internal relative humidity

Fig. 7 shows the internal RH of the AAS-SS pastes. A general pattern of internal RH decreasing with age can be observed for all pastes. The most significant decrease of the internal RH took place within the first day. Afterwards, there was a gradual decline in the internal RH over time. This observation suggested that the self-desiccation process primarily occurred in the early hydration stages within the AAS paste. The decrease in the internal RH directly resulted in the development of autogenous shrinkage (Fig. 5), suggesting that the self-desiccation is the primary mechanism of the autogenous shrinkage, as confirmed by previous studies [15]. The 7 d internal RH of 100BFS stabilized at approximately 58.3 %. In case the BFS was replaced by 15 % SS, a higher internal RH of 7 d AAS paste at 60.6 % was found. A further increase of the BFS substitution by 30 % SS, the 7 d internal RH of AAS paste reached around 61.5 %. When the replacement of BFS was increased up to a high level of 45 % SS, the AAS paste exhibited the highest 7 d internal RH at 67.3 %. The higher degree of hydration reaction resulted in larger water consumption, leading to lower internal RH values in the AAS pastes.

3.6. Compressive strength

Fig. 8 displays the compressive strength of AAS-SS pastes at the ages from 1 d to 28 d. It is evident that the SS incorporation resulted in a decrease of the compressive strength of AAS pastes. Such decrease was

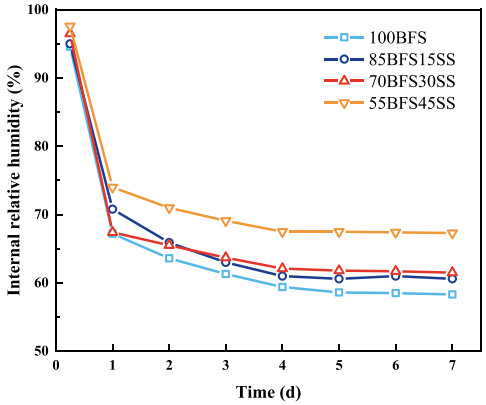

Fig. 7. Evolution of internal relative humidity inside the AAS-SS pastes.

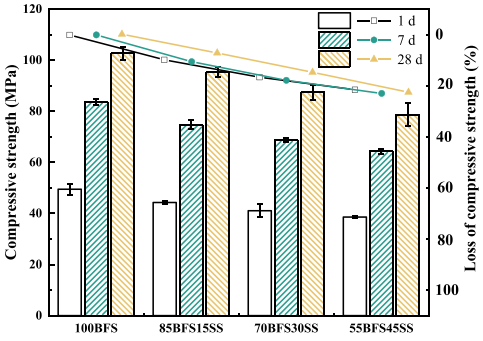

Fig. 8. Compressive strength of AAS-SS pastes.

relatively small for AAS pastes at 1 d while became particularly pronounced after 28 d. The 7 d compressive strength was reduced by 10.6 %, 17.8 % and 23.1 % for AAS pastes with the SS content of 15 %, 30 % and 45 %, respectively. It is noteworthy that the variation in strength among these mixtures at 28 d is less than 22 %. It is recognized that the variation of compressive strength is closely linked with the fineness of pore structure. The introduction of SS resulted in a coarser pore size distribution and such dilution effect was more noticeable in the later stages compared to the earlier ones, as will be analyzed in the following sections. In addition, changes in the gel structure also affect compressive strength. Zhou et al. [46] pointed out that the calcium-silicon ratio of alkali-activated SS system was significantly increased with a higher SS content, or with a decrease in BFS content. This suggested that fewer and weaker Si-O-Si bonds were formed in the C-A-S-H gels, thereby reducing the compressive strength. It is important to highlight that the compressive strength of AAS including SS as high as 45 % can still possess a reasonably high strength of 80 MPa after 28 d hydration.

3.7. Microstructure

3.7.1. XRD analysis

Fig. 9 presents the XRD patterns of AAS-SS pastes. For the 100BFS mixture, the peaks at 29.4° and 49.6° (indicated by dotted lines) suggest the production of C-A-S-H type gels [47]. However, the intensities of these peaks were lower in AAS pastes containing SS. Characteristic diffraction peaks of calcite ($CaCO_3$, PDF# 05–0586) were also observed in all samples, probably resulting from carbonation. Additionally, the presence of C_2S and RO phases is observed in the samples including SS and their contents are increased with a rise in the SS incorporations. The very slow hydration process of C_2S, as well as the inert nature of RO phases, is therefore demonstrated. The main band (2θ=29.4°) of C-A-S-H gel in 100BFS becomes denser as the curing age increases, suggesting that more amorphous hydration products are produced. Notably, for samples 85BFS15SS, 70BFS30SS and 55BFS45SS, the peak intensity representing the C-A-S-H gel was consistently lower compared to that of 100BFS at all ages. It is concluded that greater SS content may cause a reduction in the formation of C-A-S-H gel during the first 7 d.

3.7.2. TG analysis

The TG/DTG results for AAS-SS pastes are presented in Fig. 10. Three peaks of heat release are clearly noticed in the DTG curves. The main exothermic peak between 30 and 220 °C indicates the dehydration of C-A-S-H gels. The evaporation of physically bound water also contributes to the mass loss in such low temperature range. Another two small peaks associated with insignificant heat flow occurring in the temperature range 275–425 °C and 550–700 °C correspond to the decomposition of hydrotalcite-like phases and calcium carbonate, respectively [17]. The self-desiccation process of AAS pastes gradually consumes internal capillary free water, which is converted into chemically bound water within the primary hydration products. Following the mass loss within the respective temperature ranges, the amount of hydration products can be calculated, as shown in Table 5. The amount of the main hydration product, C-A-S-H gel, is 3–4 times higher than that of the hydrotalcite-like phase. With an increase in SS content, the amount of C-A-S-H gel decreases. This finding aligns with the compressive strength results, as greater mass loss signifies more hydration products.

3.7.3. Pore structure analysis

The pore structure results of 100BFS and 55BFS45SS after 1 d and 7 d, as representative, are presented in Fig. 11. The pore sizes as detected in the nitrogen adsorption tests ranged from 2 nm to 100 nm. The pore size distributions of both mixtures commonly show one main big bump, corresponding to the gel pore family. At 1 d, the critical pore size corresponding to the gel peak was 5 nm for 100BFS while it was reduced to a slightly smaller value of 3.5 nm after 7 d. However, as a comparison for 55BFS45SS, the critical pore size exhibited a significant decrease from 10 nm at 1 d to 4.5 nm at 7 d. These results are precisely consistent with the autogenous shrinkage measurements as given previously in Fig. 5. The AAS samples possessed very low-strength at the age of 1 d and meanwhile their resistance against capillary pressure was low. A coarse pore structure, especially the presence of large capillary pores, is a necessity to properly control autogenous shrinkage at the early age. Noteworthy, a substantial refinement of pore structure until the late age of 7 d would not induce a significant autogenous shrinkage, while ensuring a reasonable strength in the meantime. Accordingly, the introduction of SS into AAS enabled to produce a microstructure of low autogenous shrinkage but without a compromise in the mechanical behaviors.

With the increase of age, the pore sizes of both mixtures shifted towards smaller pores, a result of continuous hydration and

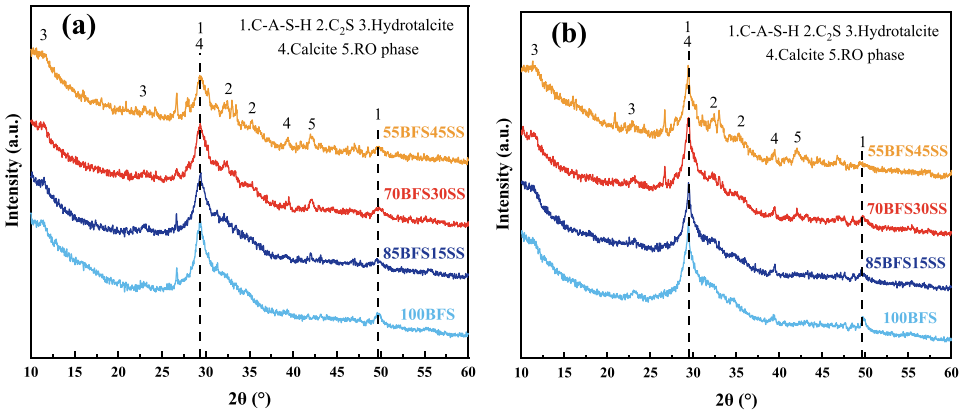

Fig. 9. XRD patterns of AAS-SS pastes cured for (a) 1 d and (b) 7 d.

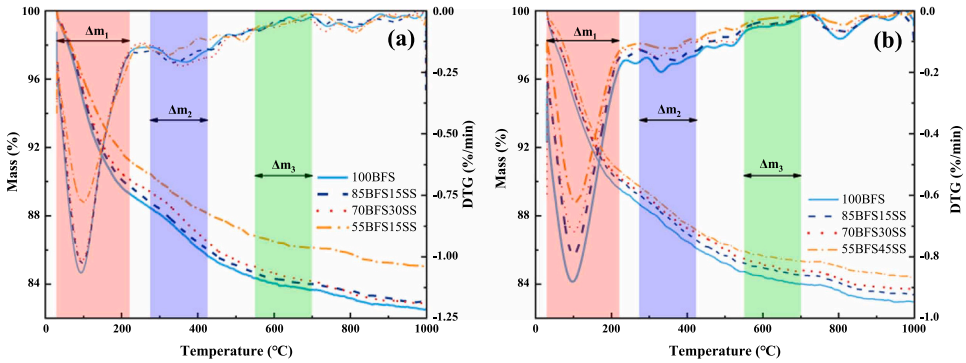

Fig. 10. TG/DTG curves of AAS-SS pastes cured for (a) 1 d and (b) 7 d.

Table 5
Mass loss of AAS-SS pastes at 30–220 ℃ (Δm_1) and 275–425 ℃ (Δm_2).

Mix ID	Samples cured for 1 d			Samples cured for 7 d		
	Δm_1 (%)	Δm_2 (%)	$\Delta m_1 + \Delta m_2$ (%)	Δm_1 (%)	Δm_2 (%)	$\Delta m_1 + \Delta m_2$ (%)
100BFS	10.66	2.80	13.46	10.38	2.56	12.94
85BFS15SS	10.23	2.79	13.02	9.86	2.65	12.51
70BFS30SS	9.82	2.94	12.76	9.69	2.48	12.17
55BFS45SS	8.70	2.34	11.04	9.30	2.57	11.87

microstructure densification. Compared to the 100BFS, the 55BFS45SS exhibits a coarser pore size distribution. This was particularly the case in the early hydration age of 1 d when the gel pores predominantly occupied the entire pore size distribution of 100BFS, but a considerable amount of capillary pores above 10 nm can be found in 55BFS45SS. The shortage of capillary pores and the dominant presence of small size gel pores jointly contributed to the pronounced development of autogenous shrinkage of 100BFS. In comparison, the presence of relatively large size capillary pores by introducing the poorly reactive SS significantly alleviated the autogenous shrinkage of 55BFS45SS at the early age. The increase of pore volume and associated coarse pore size distribution with the addition of SS were in line with heat release data and also with those reported in literature [40]. Finer pore structure tends to result in smaller meniscus radii and higher pore pressures that contribute to autogenous shrinkage, as will be described in Section 4.2.

3.8. Environmental and cost assessment

Table 6 displays the CO_2 emissions and expenses related to the raw materials utilized in this study. The results were obtained based on the data of Table 3, in addition to literature studies and market surveys [48, 49]. The CO_2 emissions of BFS (101.9 kg/ton) are higher than those of SS (36.2 kg/ton). Similarly, the cost of the mixtures using BFS tends to be higher than those with SS. It is therefore considered that using less BFS is crucial for AAS-SS to achieve sustainability with low CO_2 emissions and low total costs.

Fig. 12 shows the calculated environmental and economic impacts of

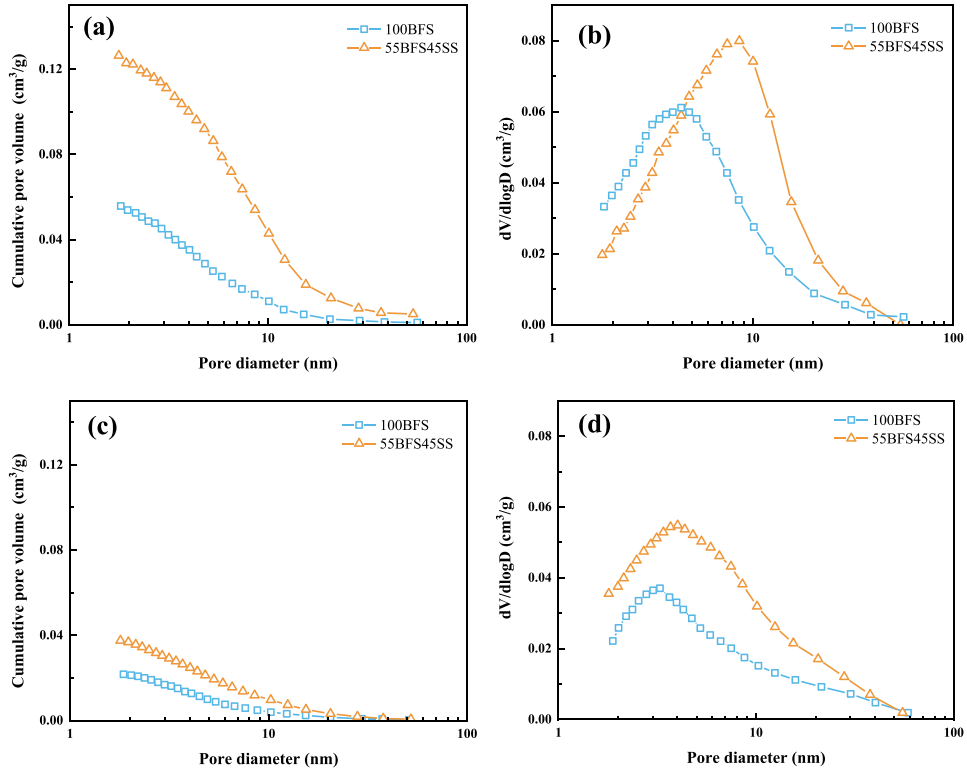

Fig. 11. Pore volume and pore size distribution curves of 100BFS and 55BFS45SS pastes: (a) and (b) for samples at 1 d while (c) and (d) for samples at 7 d.

Table 6
Carbon emissions and cost of raw materials.

Raw materials	CO_2 emission (kg/t)	Cost ($/t)	Note
BFS	101.9	38.6	-
SS	36.2	12.1	-
Na_2SiO_3	430.0	295.0	* LMP
NaOH	633.0	413.0	* LMP
Water	0.9	0.3	* LMP

* LMP: Local market prices.

the AAS-SS mixtures. It is clear that substituting BFS by 45 % SS reduces CO_2 emissions by 18.4 kg/m^3 and meanwhile decreases the autogenous shrinkage by 42 % (Fig. 12a). Following previous reports [50], an indicator associated with setting time is employed to further assess the economic benefits brought by the introduction of SS:

$$T_p = \frac{\text{Cost}}{T_{\text{initial}}} \tag{9}$$

where T_p ($/m^3·min) represents the cost per minute for materials, *Cost* ($/m^3) represents the total cost of 1 m^3 mixture, and T_{initial} (min) represents the initial setting time.

Fig. 12b shows the results of T_p calculations for AAS samples containing SS. As mentioned earlier, the introduction of SS significantly prolongs the setting time. The production cost per cubic meter of the AAS mixture decreases with increasing SS content. Notably, the T_p value of 55BFS45SS is reduced by 58.5 % compared to that of 100BFS. Extending the workability of AAS by the introduction of SS is therefore feasible in terms of both economic and environmental viewpoints.

4. Discussion

4.1. Shrinkage mechanism of AAS pastes

Fig. 13 (a) and (b) show the correlation between heat flow and autogenous shrinkage in 100BFS and 55BFS45SS, respectively. The first-order derivatives of autogenous shrinkage are provided to reveal its variation over hydration period. The inflection point of the cumulative autogenous shrinkage curve, corresponding to the peak of shrinkage rate, aligns closely with the peak of heat release rate. The autogenous shrinkage process of AAS pastes is categorized into three periods: (a) dissolution, (b) acceleration and (c) steady. The dissolution period represents the wetting of the precursor in contact with the alkaline activator and initial particle dissolution. Native C-A-S-H and C-N-A-S-H gels were produced during this period of deceleration [51]. The autogenous shrinkage values of 100BFS and 55BFS45SS during this period were approximately 86 μm/m and 54 μm/m, respectively. Using the final setting time as the "time-zero" for autogenous shrinkage of AAS pastes may be controversial. As reported in the literature [52], the final setting time of AAS paste could be attributed to the loss of workability caused by hydration products forming in voids. The "time-zero" refers to the moment when the internal RH starts to decrease, and a rapid increase in autogenous shrinkage is anticipated. Adopting the commencement of the acceleration period as the "time-zero" for autogenous shrinkage appears more convincing. During the acceleration period, the formation of C-A-S-H and C-N-A-S-H gels as the primary binding phase leads to a dramatic increase in heat flow in the pastes 100BFS and 55BFS45SS. This results in the substantial water consumption and hence the generation of capillary pores, along with decreasing internal RH and meniscus formation, known as the self-desiccation process. Consequently, autogenous shrinkage in 100BFS accelerates rapidly, exceeding 4100 μm/m by the end of this period.

In view of the sharp decrease of autogenous shrinkage, as indicated by dashed lines, the heat flow of the 55BFS45SS starts to decrease at a moment later than that of the 100BFS. This suggests that SS addition decreases the free water consumption in the entire hydrating system, mitigating the self-desiccation and capillary pressure formation, a point to be confirmed in Section 4.2. The autogenous shrinkage of 55BFS45SS is approximately 2200 μm/m, representing a 46.3 % reduction compared to that of 100BFS during this period. Subsequently, the heat flow of 55BFS45SS decreases at a lower rate and gradually a steady period commences due to a diffusion-controlled slow reaction process. Autogenous shrinkage rate decelerates and stabilizes gradually for both pastes. Thereafter the internal RH continues to decrease as the capillary water is depleted (Fig. 7), thereby sustaining capillary pressure and driving the progression of autogenous shrinkage. However, the relatively high solid skeleton stiffness limits the development of autogenous shrinkage during this period [29]. Noteworthy, the autogenous shrinkage remains significantly lower in 55BFS45SS than in 100BFS at the late stage.

4.2. Shrinkage under capillary pressure

The capillary pressure induced by the gas-liquid interface is recognized as a key factor driving autogenous shrinkage [16]. The capillary pressure theory, extensively applied to explain the shrinkage phenomenon in cementitious materials exposed to RH exceeding 40 %, serves as a main origin responsible for autogenous shrinkage in the AAS. Under sealed conditions, the alkaline reaction within hardened AAS pastes gradually depletes free capillary pore solution. As a result, the decrease in the size of water-filled pores is expected, forming a gas-liquid meniscus. Meanwhile the capillary pore pressure is generated onto the matrix, resulting in shrinkage deformation. The capillary pressure σ_{cap} can be performed using Laplace's and Kelvin's equation (Eqs. 2 and 3), as detailed below:

$$\sigma_{\text{cap}} = -\frac{2\gamma\cos\theta}{r} \tag{2}$$

$$r = \frac{2\gamma V_{\text{W}}\cos\theta}{\ln(RH_{\text{K}})RT} \tag{3}$$

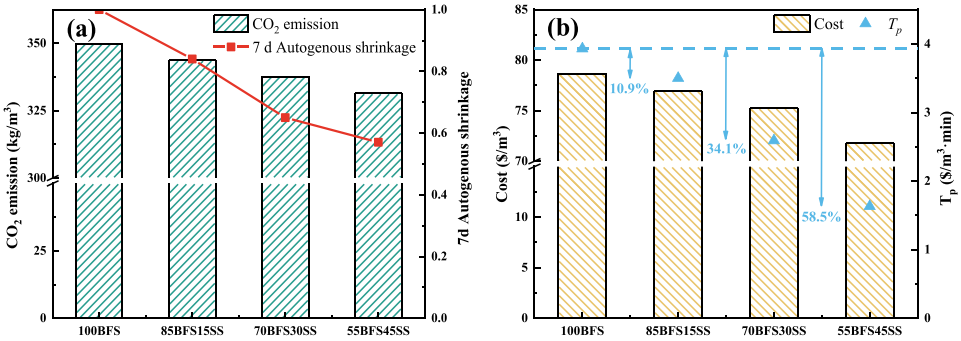

Fig. 12. The calculated (a) environmental and (b) economic impacts of the AAS-SS mixtures.

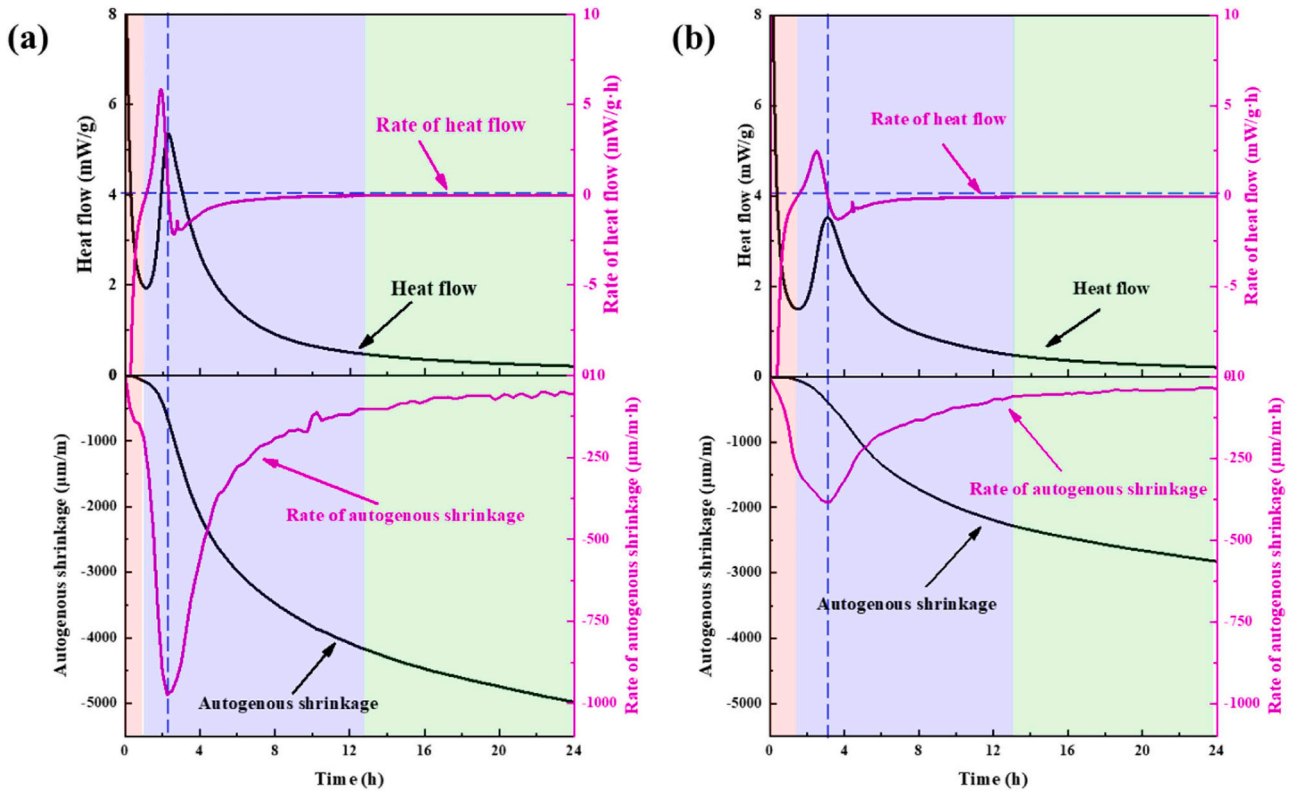

Fig. 13. Correlation between heat flow and autogenous shrinkage in (a) 100BFS and (b) 55BFS45SS.

where γ (N/m) is the surface tension, θ (°) is the contact angle, r (m) is the Kelvin radius, V_W is the molar volume, $R = 8.314$ J/(mol·K) is the universal gas constant, $T = 293.15$ K is the absolute temperature and RH_K is the internal RH caused by the meniscus curvature effect.

Based on previous reports [51], the development of internal RH is influenced not only by the curvature of the fluid/vapor meniscus but also by the water activity of the pore solution. Ion dissolution in the pore solution results in a decrease in its water activity, thereby causing a reduction in internal RH. Therefore, RH_K can be determined using Eq. (4):

$$RH_K = \frac{RH}{RH_S} \tag{4}$$

where RH is the internal relative humidity in the pore structure and RH_S is the relative humidity caused by dissolved salts and it is estimated by Raoul's law in Eq. (5):

$$RH_S = \frac{n_{H_2O}}{n_{solution}} \tag{5}$$

where n_{H_2O} and $n_{solution}$ are the number of moles of water and solution, respectively. It is important to note that RH_S can be treated as a constant less than 1, as it undergoes minimal variation throughout the self-desiccation process [17]. As a result, the value of RH_K is a proportional amplification of the RH value.

The capillary pore pressure as seen in Eq. (6) can be obtained by combining Eq. (2)~(5). Lura [53] highlighted that the impact of ions on V_W was minor. Consequently, V_W can then be set as the pure water, i.e., 18.02×10^{-6} m^3/mol, for capillary pore pressure computation. Fig. 14 gives the calculated results of the capillary pore pressure. As indicated, the pore pressure of AAS paste decreases with higher SS content, whereby the autogenous shrinkage of AAS paste is reduced. The capillary pore pressures formed within 7 d for the mixture 100BFS are approximately 1.09, 1.13 and 1.46 times those of the mixtures 85BFS15SS, 70BFS30SS and 55BFS45SS, respectively. This aligns well

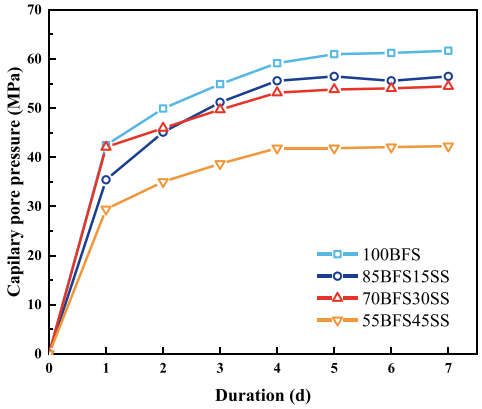

Fig. 14. The calculated capillary pore pressure of AAS-SS pastes.

with the autogenous shrinkage measurements, where the 100BFS exhibits approximately 1.19, 1.53 and 1.73 times higher autogenous shrinkage than the 85BFS15SS, 70BFS30SS and 55BFS45SS, respectively. The autogenous shrinkage seems to be mainly a result of the capillary pore pressure generated by self-desiccation. Nevertheless, the autogenous shrinkage clearly varies in response to different SS substitutions in view of the relationship between capillary pore pressure and autogenous shrinkage, as established in Fig. 15. It is suggested that extra factors besides capillary pore pressure are involved in the autogenous shrinkage of AAS pastes.

$$\sigma_{cap} = -\frac{\ln(RH_K)RT}{V_W} \tag{6}$$

In reality, the desiccation potential of AAS systems depends partly on the evolution of chemical shrinkage [53]. As the reaction progresses, the volume of the overall system decreases and resulting in the formation of

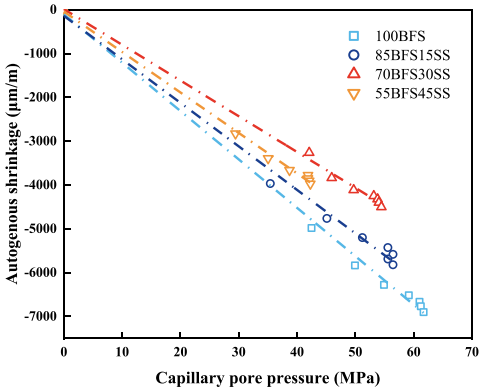

Fig. 15. The relationship between capillary pore pressure and autogenous shrinkage for AAS-SS pastes.

extra voids that are filled with gases such as air and water vapor. Gradual depletion of pore liquid from larger to smaller pores reduces the curvature radius of the meniscus, thereby inducing the pronounced formation of capillary pore pressure. The addition of SS to AAS pastes reduces the chemical shrinkage (Fig. 6), consequently decreasing the volume occupied by the gases within the pastes. The lower chemical shrinkage, together with the coarser pore structure (Fig. 11), results in a larger meniscus radius in the AAS-SS pastes compared to the reference AAS pastes at the same age, leading to lower capillary pore pressures of AAS-SS pastes. The relatively larger internal RH of AAS-SS pastes has been confirmed as from the results shown in Fig. 7. The lower RH_K values corresponding to smaller Kelvin radius are the main reason for lower internal RH values and hence for the larger capillary pore pressures.

4.3. Calculation of autogenous shrinkage

The Mackenzie-Bentz equation given in Eq. (7) was employed to calculate the autogenous shrinkage [54]. It was assumed that the deformation of AAS pastes under capillary pressure followed an elastic behavior.

$$\varepsilon_{elas} = \frac{S\sigma_{cap}}{3}\left(\frac{1}{K} - \frac{1}{K_S}\right) \tag{7}$$

where S is the saturation fraction of the paste calculated from the non-evaporated water content and chemical shrinkage [44] and the results are shown in Table 7, σ_{cap} (MPa) is the capillary pore pressure as depicted in Fig. 14, K (MPa) is the bulk modulus of the paste, and K_S = 44,000 MPa is the bulk modulus of the solid material [16].

The bulk modulus K of the AAS-SS pastes was determined by Eq. (8):

$$K = \frac{E}{3(1-2\upsilon)} \tag{8}$$

where E (MPa) is the elastic modulus of AAS-SS pastes and υ=0.15 is the Poisson's ratio [44].

The elastic modulus of AAS-SS pastes is depicted in Fig. 16. A slight decrease in elastic modulus is observed as the SS content increases. This observation can be attributable to the dual effects induced by SS addition. On the one hand, the addition of SS reduces the reactivity of hydrating system and fewer hydration products are precipitated in the

Table 7
Saturation degree of AAS-SS pastes.

Mix ID	100BFS	85BFS15SS	70BFS30SS	55BFS45SS
1 d	0.919	0.946	0.964	0.968
7 d	0.879	0.914	0.927	0.942

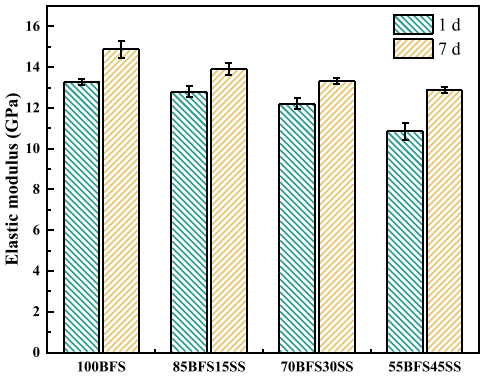

Fig. 16. Elastic modulus of AAS-SS pastes.

microstructure, leading to a coarser pore structure, known as dilution effect. On the other hand, the retarding of hydration in the alkali-activated system obviously lowers the possibility of microcracking initiation, a beneficial effect that promotes strength development. The microcracking, which is detrimental but hardly unavoidable for AAS systems owing to the very quick hydration process at the early age, could be increasingly reduced by using more SS. The various AAS-SS systems under study exhibit therefore very similar elastic modulus.

Fig. 17 shows the autogenous shrinkage of AAS-SS pastes calculated using Eq. (7)~(8). It is evident that the simulated autogenous shrinkage at 7 d for 100BFS, 85BFS15SS, 70BFS30SS and 55BFS45SS are approximately 1272, 1121, 1026 and 828 μm/m, respectively. Compared to the measured autogenous shrinkage, the calculated values for the four mixtures at 7 d are lower by factors of 5.4, 5.2, 4.3 and 4.8, respectively. This aligns with the findings reported in the literature for OPC paste [55], namely that the calculated autogenous shrinkage is reduced by a factor of about 5.5 compared to the measured value. A similar statement has been claimed as well by Sant et al. [56]. If only the elastic portion is considered in the calculations, the difference between the calculated and measured autogenous shrinkage values can be attributed to the visco-elastic response of OPC to the pore pressure. In fact, the deformation of the paste under sustained internal stresses (such as capillary stresses) takes effect, which resembles the creep behavior under external stresses, resulting in different autogenous shrinkage between calculations and measurements.

It is notable that while the calculated autogenous shrinkage does not align closely with the measured data, the calculated autogenous shrinkage exhibits significant differences among the four mixtures under study. Equally notable is that the calculated autogenous shrinkage of 100BFS at 1 d accounts for 76.3 % of that at 7 d. This value is precisely consistent with the measurement of the same mixture about the proportion of autogenous shrinkage (71.1 %). It is evident that the elastic

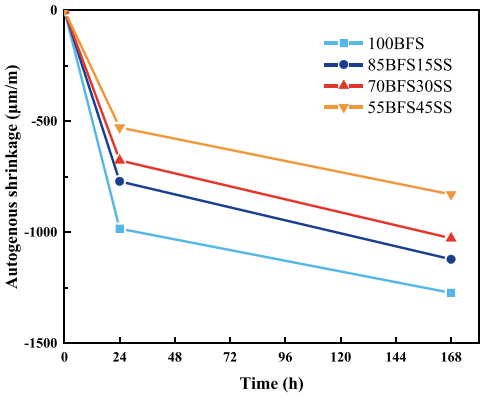

Fig. 17. Calculated autogenous shrinkage of AAS-SS pastes.

deformation of AAS paste also takes place at early stages. Apart from the capillary pressure theory, there might be other mechanisms contributing to autogenous shrinkage of AAS systems [26,57] and deserving further investigations.

5. Conclusions

This paper primarily investigates the mitigating effect of SS on the autogenous shrinkage of AAS pastes and provides new insights into the mitigation mechanism about the autogenous shrinkage. An assessment regarding the roles of adding SS in the AAS systems was conducted from the perspectives of hydration, microstructure, mechanical behavior and sustainability. A continuity of this work has been implemented to clarify the long-term performance of AAS-SS systems. Based on the results and discussion of this work, it is found that SS serves as a highly promising admixture for AAS systems. Besides, the following conclusions can be drawn.

(1) A higher SS content leads to prolongations of the setting time of AAS pastes and meanwhile a decrease of the cumulative hydration heat, along with a delay in the main exothermic peak. The evolution of autogenous shrinkage is found to correlate well with the heat flow of hydration in the AAS-SS systems.
(2) The addition of SS significantly reduces the autogenous shrinkage of AAS paste. The high-level substitution of BFS by 45 % SS results in the 7 d autogenous shrinkage of AAS paste to substantially decrease by 42 % while without a compromise in the elastic modulus and compressive strength.
(3) The mitigation of autogenous shrinkage of AAS paste in the presence of SS largely lies in its inactive components of C_2S and RO phases, which decelerate the very early hydration progress, and a compressive strength of around 80 MPa could be achieved at 28 d for the AAS paste with 45 % SS.
(4) The incorporation of SS impedes the progress of chemical shrinkage and pore structure refinement in the paste, and therefore substantially retarding the self-desiccation and capillary pressure generation. Moreover, an increase of SS reduces the initiation of microcracking and hence beneficial to strength development.
(5) The sustainability of AAS is improved with the addition of SS. The utilization of 45 % SS can reduce CO_2 emissions by 18.4 kg/m^3 while reducing the material cost per minute ($/m^3·min) by 58.5 %.

CRediT authorship contribution statement

Kang Li: Writing – original draft, Methodology, Formal analysis, Data curation. **Bruno Briseghella:** Supervision, Project administration. **Minfei Liang:** Validation, Investigation. **Demetris Nicolaides:** Supervision, Investigation. **Zhengxian Yang:** Writing – review & editing, Supervision, Funding acquisition, Conceptualization. **Yong Zhang:** Writing – review & editing, Project administration, Conceptualization. **Giuseppe Carlo Marano:** Validation, Supervision, Project administration.

Declaration of Competing Interest

The authors declare that they have no known competing financial interests or personal relationships that could have appeared to influence the work reported in this paper.

Data availability

Data will be made available on request.

Acknowledgements

This work was financially supported by Fujian Ocean and Fishery Bureau (FJHJF-L-2022-19), National Natural Science Foundation of China (51978171), Fuzhou Science and Technology Bureau (2021-P-031) and Opening Project of State Key Laboratory of Green Building Materials (2023GBM05).

References

[1] A. Kylili, P.A. Fokaides, Policy trends for the sustainability assessment of construction materials: a review, Sustain. Cities Soc. 35 (2017) 280–288, https://doi.org/10.1016/j.scs.2017.08.013.
[2] J. Xie, Z. Wu, X. Zhang, X. Hu, C. Shi, Trends and developments in low-heat Portland cement and concrete: a review, Constr. Build. Mater. 392 (2023) 131535, https://doi.org/10.1016/j.conbuildmat.2023.131535.
[3] F. Greer, P. Raftery, A. Horvath, Considerations for estimating operational greenhouse gas emissions in whole building life-cycle assessments, Build. Environ. 254 (2024) 111383, https://doi.org/10.1016/j.buildenv.2024.111383.
[4] C. Xue, V. Sirivivatnanon, A. Nezhad, Q. Zhao, Comparisons of alkali-activated binder concrete (ABC) with OPC concrete - a review, Cem. Concr. Compos. 135 (2023) 104851, https://doi.org/10.1016/j.cemconcomp.2022.104851.
[5] K. Skillington, R.H. Crawford, G. Warren-Myers, K. Davidson, A review of existing policy for reducing embodied energy and greenhouse gas emissions of buildings, Energy Policy 168 (2022) 112920, https://doi.org/10.1016/j.enpol.2022.112920.
[6] J.L. Provis, Alkali-activated materials, Cem. Concr. Res. 114 (2018) 40–48, https://doi.org/10.1016/j.jclepro.2017.07.212.
[7] Q. Fu, M. Bu, Z. Zhang, W. Xu, Q. Yuan, D. Niu, Hydration characteristics and microstructure of alkali-activated slag concrete: a review, Engineering 20 (2023) 162–179, https://doi.org/10.1016/j.eng.2021.07.026.
[8] G. Liao, D. Wang, W. Wang, Y. He, Microstructure, strength development mechanism, and CO_2 emission analyses of alkali-activated fly ash-slag mortars, J. Clean. Prod. 442 (2024) 141116, https://doi.org/10.1016/j.jclepro.2024.141116.
[9] A. Ślosarczyk, J. Fořt, I. Klapiszewska, M. Thomas, Ł. Klapiszewski, R. Černý, A literature review of the latest trends and perspectives regarding alkali-activated materials in terms of sustainable development, J. Mater. Res. Technol. 25 (2023) 5394–5425, https://doi.org/10.1016/j.jmrt.2023.07.038.
[10] T. Luukkonen, Z. Abdollahnejad, J. Yliniemi, P. Kinnunen, M. Illikainen, One-part alkali-activated materials: a review, Cem. Concr. Res. 103 (2018) 21–34, https://doi.org/10.1016/j.cemconres.2017.10.001.
[11] V. Bílek Jr, R. Novotný, J. Koplík, M. Kadlec, L. Kalina, Philosophy of rational mixture proportioning of alkali-activated materials validated by the hydration kinetics of alkali-activated slag and its microstructure, Cem. Concr. Res. 168 (2023) 107139, https://doi.org/10.1016/j.cemconres.2023.107139.
[12] X. Ji, Z. Wang, X. Wang, X. Zhao, H. Zhang, T. Zhang, Microstructures and properties of alkali-activated slags with composite activator: effects of Na_2O equivalents, J. Clean. Prod. 450 (2024) 141754, https://doi.org/10.1016/j.jclepro.2024.141754.
[13] Q. Li, Z. Ren, X. Su, Y. Feng, T. Xu, Z. Zheng, P. Li, Improving sulfate and chloride resistance in eco-friendly marine concrete: alkali-activated slag system with mineral admixtures, Constr. Build. Mater. 411 (2024) 134333, https://doi.org/10.1016/j.conbuildmat.2023.134333.
[14] D. Jiang, C. Shi, Z. Zhang, Recent progress in understanding setting and hardening of alkali-activated slag (AAS) materials, Cem. Concr. Compos 134 (2022) 104795, https://doi.org/10.1016/j.cemconcomp.2022.104795.
[15] Z. Li, Y. Chen, J.L. Provis, Ö. Cizer, G. Ye, Autogenous shrinkage of alkali-activated slag: a critical review, Cem. Concr. Res. 172 (2023) 107244, https://doi.org/10.1016/j.cemconres.2023.107244.
[16] Z. Li, T. Lu, X. Liang, H. Dong, G. Ye, Mechanisms of autogenous shrinkage of alkali-activated slag and fly ash pastes, Cem. Concr. Res. 135 (2020) 106107, https://doi.org/10.1016/j.cemconres.2023.107244.
[17] W. Chen, B. Li, J. Wang, N. Thom, Effects of alkali dosage and silicate modulus on autogenous shrinkage of alkali-activated slag cement paste, Cem. Concr. Res. 141 (2021) 106322, https://doi.org/10.1016/j.cemconres.2020.106322.
[18] L. Wu, N. Farzadnia, C. Shi, Z. Zhang, H. Wang, Autogenous shrinkage of high performance concrete: a review, Constr. Build. Mater. 149 (2017) 62–75, https://doi.org/10.1016/j.conbuildmat.2017.05.064.
[19] L. Barcelo, M. Moranville, B. Clavaud, Autogenous shrinkage of concrete: a balance between autogenous swelling and self-desiccation, Cem. Concr. Res. 35 (2005) 177–183, https://doi.org/10.1016/j.cemconres.2004.05.050.
[20] F. Collins, J. Sanjayan, Effect of pore size distribution on drying shrinking of alkali activated slag concrete, Cem. Concr. Res. 30 (2000) 1401–1406, https://doi.org/10.1016/S0008-8846(00)00327-6.
[21] D.B. Kumarappa, S. Peethamparan, M. Ngami, Autogenous shrinkage of alkali activated slag mortars: basic mechanisms and mitigation methods, Cem. Concr. Res. 109 (2018) 1–9, https://doi.org/10.1016/j.cemconres.2018.04.004.
[22] C. Cartwright, F. Rajabipour, A. Radlińska, Shrinkage characteristics of alkali-activated slag cements, J. Mater. Civil. Eng. 27 (2015) B4014007, https://doi.org/10.1061/(ASCE)MT.1943-5533.0001058.
[23] C. Song, Y.C. Choi, S. Choi, Effect of internal curing by superabsorbent polymers-internal relative humidity and autogenous shrinkage of alkali-activated slag

mortars, Constr. Build. Mater. 123 (2016) 198–206, https://doi.org/10.1016/j.conbuildmat.2016.07.007.
[24] X. Liu, B. Li, Y.T. Chen, B. Ghiassi, Microstructure refinement and shrinkage mitigation of alkali-activated slag paste by superabsorbent polymer, Constr. Build. Mater. 375 (2023) 130884, https://doi.org/10.1016/j.conbuildmat.2023.130884.
[25] Z. Yang, P. Shi, Y. Zhang, Z. Li, Effect of superabsorbent polymer introduction on properties of alkali-activated slag mortar, Constr. Build. Mater. 340 (2022) 127541, https://doi.org/10.1016/j.conbuildmat.2022.127541.
[26] W. Tu, Y. Zhu, G. Fang, X. Wang, M. Zhang, Internal curing of alkali-activated fly ash-slag pastes using superabsorbent polymer, Cem. Concr. Res. 116 (2019) 179–190, https://doi.org/10.1016/j.cemconres.2018.11.018.
[27] A.R. Sakulich, D.P. Bentz, Mitigation of autogenous shrinkage in alkali activated slag mortars by internal curing, Mater. Struct. 46 (2013) 1355–1367, https://doi.org/10.1617/s11527-012-9978-z.
[28] S. Oh, Y.C. Choi, Superabsorbent polymers as internal curing agents in alkali activated slag mortars, Constr. Build. Mater. 159 (2018) 1–8, https://doi.org/10.1016/j.conbuildmat.2017.10.121.
[29] D. Jiang, X. Li, Y. Lv, C. Li, W. Jiang, Z. Liu, J. Dan, Autogenous shrinkage and hydration property of alkali activated slag pastes containing superabsorbent polymer, Cem. Concr. Res. 149 (2021) 106581, https://doi.org/10.1016/j.cemconres.2021.106581.
[30] H. Ye, A. Radlińska, Shrinkage mitigation strategies in alkali-activated slag, Cem. Concr. Res. 101 (2017) 131–143, https://doi.org/10.1016/j.cemconres.2017.08.025.
[31] S. Uppalapati, L. Vandewalle, Ö. Cizer, Autogenous shrinkage of slag-fly ash blends activated with hybrid sodium silicate and sodium sulfate at different curing temperatures, Constr. Build. Mater. 265 (2020) 121276, https://doi.org/10.1016/j.conbuildmat.2020.121276.
[32] L. Chen, H. Wang, K. Zheng, J. Zhou, F. He, Q. Yuan, The mechanism of basic oxygen furnace steel slag retarding early-age hydration of Portland cement and mitigating approach towards higher utilization rate, J. Clean. Prod. 362 (2022) 132493, https://doi.org/10.1016/j.jclepro.2022.132493.
[33] G. Liu, H. Rong, J. Wang, Valorization of converter steel slag in sustainable mortars by a combined alkali and carbonation activation, J. Clean. Prod. 370 (2022) 133519, https://doi.org/10.1016/j.jclepro.2022.133519.
[34] J. Liu, H. Jing, Z. Wang, X. Wang, L. Zhang, Recycling of steel slag in sustainable bituminous mixtures: self-healing performance, mechanism, environmental and economic analyses, J. Clean. Prod. 429 (2023) 139496, https://doi.org/10.1016/j.jclepro.2023.139496.
[35] S. Zhuang, Q. Wang, Inhibition mechanisms of steel slag on the early-age hydration of cement, Cem. Concr. Res. 140 (2021) 106283, https://doi.org/10.1016/j.cemconres.2020.106283.
[36] Q. Wang, M. Shi, J. Yang, Influence of classified steel slag with particle sizes smaller than 20 μm on the properties of cement and concrete, Constr. Build. Mater. 123 (2016) 601–610, https://doi.org/10.1016/j.conbuildmat.2016.07.042.
[37] Y. Liu, Z. Zhang, G. Hou, P. Yan, Preparation of sustainable and green cement-based composite binders with high-volume steel slag powder and ultrafine blast furnace slag powder, J. Clean. Prod. 289 (2021) 125133, https://doi.org/10.1016/j.jclepro.2020.125133.
[38] N. You, B. Li, R. Cao, J. Shi, C. Chen, Y. Zhang, The influence of steel slag and ferronickel slag on the properties of alkali-activated slag mortar, Constr. Build. Mater. 227 (2019) 116614, https://doi.org/10.1016/j.conbuildmat.2019.07.340.
[39] J. Deng, X. Zhu, D. Xiong, Q. Li, C. Yang, K. Yang, M. Basheer, Mitigation of autogenous shrinkage of alkali-activated slag mortar by stearate salts, Constr. Build. Mater. 384 (2023) 131383, https://doi.org/10.1016/j.conbuildmat.2023.131383.
[40] S. Ghorbani, L. Stefanini, Y. Sun, B. Walkley, J.L. Provis, G. De Schutter, S. Matthys, Characterisation of alkali-activated stainless steel slag and blast-furnace slag cements, Cem. Concr. Compos. 143 (2023) 105230, https://doi.org/10.1016/j.cemconcomp.2023.105230.
[41] E.P. Barrett, L.G. Joyner, P.P. Halenda, The determination of pore volume and area distributions in porous substances. I. Computations from nitrogen isotherms, J. Am. Chem. Soc. 73 (1951) 373–380.
[42] G.F. Huseien, K.W. Shah, Durability and life cycle evaluation of self-compacting concrete containing fly ash as GBFS replacement with alkali activation, Constr. Build. Mater. 235 (2020) 117458, https://doi.org/10.1016/j.conbuildmat.2019.117458.
[43] W. Song, Z. Zhu, Y. Peng, Y. Wan, X. Xu, S. Pu, Y. Wei, Effect of steel slag on fresh, hardened and microstructural properties of high-calcium fly ash based geopolymers at standard curing condition, Constr. Build. Mater. 229 (2019) 116933, https://doi.org/10.1016/j.conbuildmat.2019.116933.
[44] Z. Li, M. Nedeljković, B. Chen, G. Ye, Mitigating the autogenous shrinkage of alkali-activated slag by metakaolin, Cem. Concr. Res. 122 (2019) 30–41, https://doi.org/10.1016/j.cemconres.2019.04.016.
[45] N.K. Lee, J.G. Jang, H.K. Lee, Shrinkage characteristics of alkali-activated fly ash/slag paste and mortar at early ages, Cem. Concr. Compos. 53 (2014) 239–248, https://doi.org/10.1016/j.cemconcomp.2014.07.007.
[46] Y. Zhou, J. Sun, Y. Liao, Influence of ground granulated blast furnace slag on the early hydration and microstructure of alkali-activated converter steel slag binder, J. Therm. Anal. Calorim. 147 (2022) 243–252, https://doi.org/10.1007/s10973-020-10220-0.
[47] M.B. Haha, G. Le Saout, F. Winnefeld, B. Lothenbach, Influence of activator type on hydration kinetics, hydrate assemblage and microstructural development of alkali activated blast-furnace slags, Cem. Concr. Res. 41 (2011) 301–310, https://doi.org/10.1016/j.cemconres.2010.11.016.
[48] E. Ozcelikci, A. Kul, M.F. Gunal, B.F. Ozel, G. Yildirim, A. Ashour, M. Sahmaran, A comprehensive study on the compressive strength, durability-related parameters and microstructure of geopolymer mortars based on mixed construction and demolition waste, J. Clean. Prod. 396 (2023) 136522, https://doi.org/10.1016/j.jclepro.2023.136522.
[49] GB/T 51366, Standard for Building Carbon Emission Calculation, 2019. https://www.chinesestandard.net/Related.aspx/GBT51366-2019.
[50] X. Ma, Y. Zhao, M. Liu, Y. Xia, Y. Yang, Sodium gluconate as a retarder modified sewage sludge ash-based geopolymers: mechanism and environmental assessment, J. Clean. Prod. 419 (2023) 138317, https://doi.org/10.1016/j.jclepro.2023.138317.
[51] H. Chen, M. Wyrzykowski, K. Scrivener, P. Lura, Prediction of self-desiccation in low water-to-cement ratio pastes based on pore structure evolution, Cem. Concr. Res. 49 (2013) 38–47, https://doi.org/10.1016/j.cemconres.2013.03.013.
[52] A. Fernández-Jiménez, F. Puertas, Effect of activator mix on the hydration and strength behaviour of alkali-activated slag cements, Adv. Cem. Res. 15 (2003) 129–136, https://doi.org/10.1680/adcr.2003.15.3.129.
[53] P. Lura, Autogenous Deformation and Internal Curing of Concrete, PhD thesis, Delft University of Technology, 2003.
[54] D.P. Bentz, E.J. Garboczi, D.A. Quenard, Modelling drying shrinkage in reconstructed porous materials: application to porous Vycor glass, Model. Simul. Mater. Sci. Eng. 6 (1998) 211, https://doi.org/10.1088/0965-0393/6/3/002.
[55] W. Zuo, P. Feng, P. Zhong, Q. Tian, N. Gao, Y. Wang, C. Miao, Effects of novel polymer-type shrinkage-reducing admixture on early age autogenous deformation of cement pastes, Cem. Concr. Res. 100 (2017) 413–422, https://doi.org/10.1016/j.cemconres.2017.08.007.
[56] G. Sant, B. Lothenbach, P. Juilland, G. Le Saout, J. Weiss, K. Scrivener, The origin of early age expansions induced in cementitious materials containing shrinkage reducing admixtures, Cem. Concr. Res. 41 (2011) 218–229, https://doi.org/10.1016/j.cemconres.2010.12.004.
[57] G. Fang, H. Bahrami, M. Zhang, Mechanisms of autogenous shrinkage of alkali-activated fly ash-slag pastes cured at ambient temperature within 24h, Constr. Build. Mater. 171 (2018) 377–387, https://doi.org/10.1016/j.conbuildmat.2018.03.155.